Journal of Catalysis 286 (2012) 78–87

Contents lists available at SciVerse ScienceDirect

Journal of Catalysis

journal homepage: www.elsevier.com/locate/jcat

Novel $PtCuO/CeO_2/\alpha\text{-}Al_2O_3$ sponge catalysts for the preferential oxidation of CO (PROX) prepared by means of supercritical fluid reactive deposition (SFRD)

Sebastian Lang [a], Michael Türk [b], Bettina Kraushaar-Czarnetzki [a,*]

[a] Institute of Chemical Process Engineering CVT, Karlsruhe Institute of Technology (KIT, Campus South), Kaiserstrasse 12, D-76128 Karlsruhe, Germany
[b] Institute for Technical Thermodynamics and Refrigeration, Karlsruhe Institute of Technology (KIT, Campus South), Kaiserstrasse 12, D-76128 Karlsruhe, Germany

ARTICLE INFO

Article history:
Received 29 June 2011
Revised 19 October 2011
Accepted 19 October 2011
Available online 23 November 2011

Keywords:
Platinum
Copper
CeO_2
PROX
SFRD
Ceramic sponges

ABSTRACT

Ceramic sponges (α-alumina) supporting ceria wash-coats and PtCuO layers of varying compositions were tested in the preferential oxidation (PROX) of CO in the presence of excess hydrogen. Copper and platinum were loaded simultaneously on the ceria-coated sponge by means of supercritical fluid reactive deposition (SFRD) which includes adsorption and reduction of metal-organic complexes dissolved in supercritical CO_2. Products were characterized by means of SEM, STEM HAADF, EDX, H_2-TPR, CO-TPD, CO_2-TPD and N_2-adsorption. Catalysts prepared after the SFRD-method exhibit high selectivity. The CO oxidation activity roughly correlates with the copper content and is superior as compared to the activity of PROX-catalysts reported in the literature so far.

1. Introduction

CuO/CeO_2-catalysts have many fields of application such as the combustion of CO and methane [1], the water–gas shift reaction [2–4], the reduction of SO_2 by CO [5], reduction of NO_x [6] methanol synthesis [7], and the wet oxidation of phenol [8]. Most frequently they are being investigated as catalysts for the preferential oxidation of CO in the presence of hydrogen (PROX) [9] for application in the context of a fuel cell economy.

Fuel cells find increasing proliferation due to their high efficiency in small scale power generation. In those cases in which fuel cells act as an auxiliary power sources, overall efficiency might be further increased by not making use of a dedicated hydrogen fuel tank, but by utilizing the chemical fuel (i.e., methane, methanol, petrol, diesel, etc.) already at hand and converting it to hydrogen. In this scenario, a reforming of the fuel is followed by a water–gas shift stage to increase the H_2-content of the feed. Because the CO-concentration is required to be lower than 10 ppm [10], a further purification has to be carried out, since this concentration is below the thermodynamic equilibrium concentration that could be reached at water–gas shift temperatures. The most straightforward method to achieve this goal is the preferential oxidation of CO (PROX). The PROX process is a unit operation step during which CO is selectively oxidized to CO_2 while the simultaneous oxidation of H_2 is avoided.

It is agreed upon that the dispersion of copper on ceria is the key parameter to a high catalyst activity [11–13]. In the literature, a multitude of preparation routes for CuO/CeO_2-type catalysts has been reported to date. In this present study, we apply supercritical fluid reactive deposition (SFRD) as a novel method to produce highly dispersed copper (and platinum) particles on a ceria wash-coat. Previously, SFRD has been employed to prepare Pt/SnO_2 catalysts with a high dispersion of platinum [14]. The concept is also employed to create thin metal films for optical and microelectronic applications [15]. In which case, however, an excess of the complexes melting point is sought after in order to create a film rather than separate particles.

Our method comprises dissolution of suitable metal-organic complexes in supercritical CO_2, adsorption of the complexes on the catalyst support, and *in situ* reduction in the supercritical state with dissolved hydrogen. Upon pressure relief, CO_2 is vaporized and removed together with the organic ligands and residual hydrogen. Because disturbing effects of capillary pressure and gravitation are absent, SFRD is particularly useful to achieve even distributions of metallic nanoparticles on supports of complex geometry and/or with fine pores [14,16]. We have chosen ceramic sponges as catalyst carriers because they combine low pressure drop with good heat and mass transfer characteristics [17,18].

* Corresponding author.
E-mail address: Kraushaar@kit.edu (B. Kraushaar-Czarnetzki).

0021-9517/$ - see front matter © 2011 Elsevier Inc. All rights reserved.
doi:10.1016/j.jcat.2011.10.017

2. Experimental

2.1. Catalyst preparation

The catalysts discussed here consisted of copper oxide with minor amounts of platinum deposited on ceria wash-coats. Cylindrical pieces of α-Al_2O_3 sponges with a pore density of 20 ppi provided by *Vesuvius* were used as catalyst supports. Fig. 1 shows exemplarily a blank support, a sponge with ceria wash-coat and a finished catalyst.

Wash-coating was performed with a nitrate-stabilized ceria sol with an oxide content of 20% m/m (*Nyacol*), followed by drying and calcination in air for 3 h at 400 °C. The supercritical fluid reactive deposition (SFRD) of copper and platinum was carried out in a horizontal tubular steel batch reactor equipped with a magnetic stirrer (Fig. 3). A wash-coated sponge was placed in the reactor together with the solid metal precursors copper-t-methyl-heptanedionate ($Cu(tmhd)_2$) and 2-Me–Pt(II)-cyclooctadien (2MePtCOD) (Fig. 2). After evacuation to 10 Pa, the reactor was pressurized with CO_2 to 5 MPa and heated to 80 °C. Thereafter, the pressure was slowly and isothermically raised to 15.5 MPa using a screw press (SP-1). At these conditions, CO_2 is in supercritical state, and the metal complexes are dissolved. After 20 h, the adsorption equilibrium between the supercritical solution and the ceria surface is established, and the stirrer is switched off. Subsequently, 1.12% (molar) of the CO_2 is isobarically exchanged with H_2 by pressing a defined amount of H_2 from the opposite direction into the reactor with a second screw press (SP-2) while simultaneously pulling fluid from the reactor with the first screw press (SP-1). Upon contact with the dissolved H_2, the organometallic complexes are reduced to the respective metals, and the organic ligands are dissolved in sc-CO_2. After 2 h of reduction at 80 °C, the vessel is depressurized and CO_2 together with organics are flushed out.

For the purpose of comparison, a set of catalysts was prepared via impregnation. In this case, instead of the SFRD treatment, ceria-coated sponges were dipped for 5 min into a 0.7 M $Cu(NO_3)_2$ solution.

The weight gain after SFRD treatment and also after impregnation with $Cu(NO_3)_2$ was in the range of 5–9 mg, relating to about 0.3% of the final weight. Finally, the samples were calcined in air at 450 °C for 3 h.

2.2. Catalytic performance tests

PROX experiments were carried out in an isothermal tubular plug-flow reactor made of glass. A detailed description of the reactor can be found elsewhere [17]. A flowchart of the test rig is given in Fig. 4. The temperature was measured by two radially mounted thermocouples up- and down-flow to the catalyst bed. The reactor could be bypassed to measure inlet concentrations. Concentrations of CO and CO_2 were determined on-line using an *ABB Uras14* analyzer; O_2 was measured with an *ABB Magnos26* analyzer. Volumetric flow rates were varied between 20 l_{NTP}/h and 48 l_{NTP}/h. The corresponding weight-hourly space velocities (WHSV), defined according to Eq. (1), were ranging between 0.19 $h^{-1}$and 2.1 h^{-1}.

$$\mathrm{WHSV} = \frac{\dot{m}_{\mathrm{CO}}}{m_{\mathrm{active}}} \ (\mathrm{h}^{-1}) \tag{1}$$

The active mass m_{active} of the catalyst is defined as the sum of the masses of CeO_2, Pt and CuO. It is determined by subtracting the weight of the blank α-Al_2O_3 sponge from the weight of the finished sample after calcination. The feed gas was composed of 0.5% CO, 0.5% O_2, 41% H_2, and nitrogen as the rest. The reactor temperature was varied between 90 °C and 150 °C. The conversion of CO was calculated as follows:

$$X_{\mathrm{CO}} = \frac{C_{\mathrm{CO,in}} - C_{\mathrm{CO,out}}}{C_{\mathrm{CO,in}}} \tag{2}$$

The selectivity to CO_2 was related to the oxygen consumption according to Eq. (3).

$$S_{\mathrm{CO_2,O_2}} = \frac{C_{\mathrm{CO,in}} - C_{\mathrm{CO,out}}}{2(C_{\mathrm{O_2,in}} - C_{\mathrm{O_2,out}})} \tag{3}$$

External mass transfer limitation was ruled out by employing a correlation previously devised for ceramic sponges [17]. Temperature rise on the catalytic layer has been ruled out according to the Mears heat criterion in conjunction with a heat transfer correlation on ceramic sponges presented by Dietrich et al. [19]. Internal mass transfer limitations have been ruled out by the Weisz–Prater criterion. The rate coefficient k_m is related to the active mass and serves as an activity parameter. Assuming first-order kinetics in CO according to $r_m = k_m \cdot C_{CO}$, the coefficient k_m can be calculated from the CO-conversion according to

$$k_{\mathrm{m}}\ (T) = \frac{-\ln(1 - X_{\mathrm{CO}}(T))}{\tau_{\mathrm{mod}}} \tag{4}$$

with τ_{mod} being defined as

$$\tau_{\mathrm{mod}} = \frac{\dot{V}_0}{m_{\mathrm{active}}} \tag{5}$$

2.3. Characterization

The contents of Cu, Pt, and Ce were determined by means of ICP-OES (*Varian Vista Pro CCD – Simultaneous* ICP-OES). SEM images were taken on a *LEO 1530 Gemini* microscope. BET surface areas and pore sizes of the catalyst samples were determined by means of nitrogen adsorption on a *Micromeritics ASAP2010*.

STEM HAADF images and according EDX data were obtained at a *FEI Titan 80–300 Cubed*. The sample was prepared for focused ion beam (FIB) milling at a combined SEM/FIB system (*ZEISS EsB 1540 Crossbeam*) by cutting a 5 × 10 μm cross-sectional slice from the surface layer of sample XII and consequently thinning it to about 50 nm in a Ga-ion beam.

Temperature-programmed reduction (TPR) and desorption (TPD) experiments were carried out on a *Micromeritics 2910* apparatus equipped with a thermal conductivity detector. An on-line quadrupole mass spectrometer (*Pfeiffer Vakuum QMG422*) served as an additional detector. TPR measurements were carried out at 10 °C/min in a flow rate of 25 ml_{NTP}/min of 5% H_2 in Ar after preheating in a flow of He for 1 h at 400 °C. TPD experiments were performed after preheating the sample at 450 °C in He and subsequent saturation of the sample surface with either CO_2 or CO at 30 °C. Desorption was achieved by heating in a flow of He at a rate of 2.5 °C/min with a holding step at 200 °C.

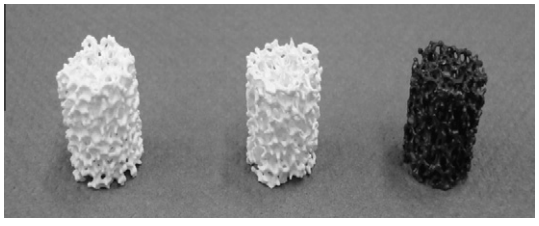

Fig. 1. Catalyst in its three stages of preparation (from left to right): blank α-Al_2O_3 sponge; yellowish after coating with CeO_2, matte black after SFRD treatment and subsequent calcination (deposition of CuO and Pt).

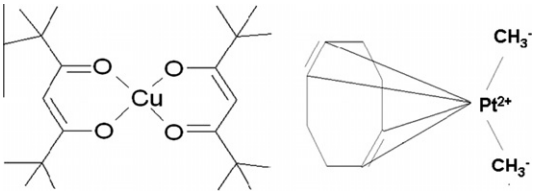

Fig. 2. Organometallic Cu and Pt precursors used for SFRD: $Cu(tmhd)_2$ (left) and 2MePt(COD) (right).

3. Results and discussion

3.1. Composition and morphology

Table 1 summarizes some properties of the samples under investigation. All specimens except for sample II were furnished with a ceria wash-coat with a thickness of 4–10 μm. The pore diameter of the ceria layer was determined via the BJH-method as 2.3 nm. It should be noted that the values in column 2 of Table 1 refer to the compositions of the active layers, only, without taking into account the mass of the sponge support.

The size distribution of 136 distinguishable particles taken from a micrograph of a ceria-coated sponge is depicted in Fig. 5. It is known from the literature that ceria particles smaller than 20 nm show an improved mobility of lattice oxygen due to a widening of the lattice [20]. Here, half of the diameters are smaller than 19 nm, indicating that a major part of the ceria washcoat should exhibit beneficial properties in the PROX application.

3.2. TPD after saturation with CO and CO_2

Fig. 6 shows desorption profiles of CO_2 after saturation of the catalyst (here: sample VI) with either CO_2 (black line) or CO (gray

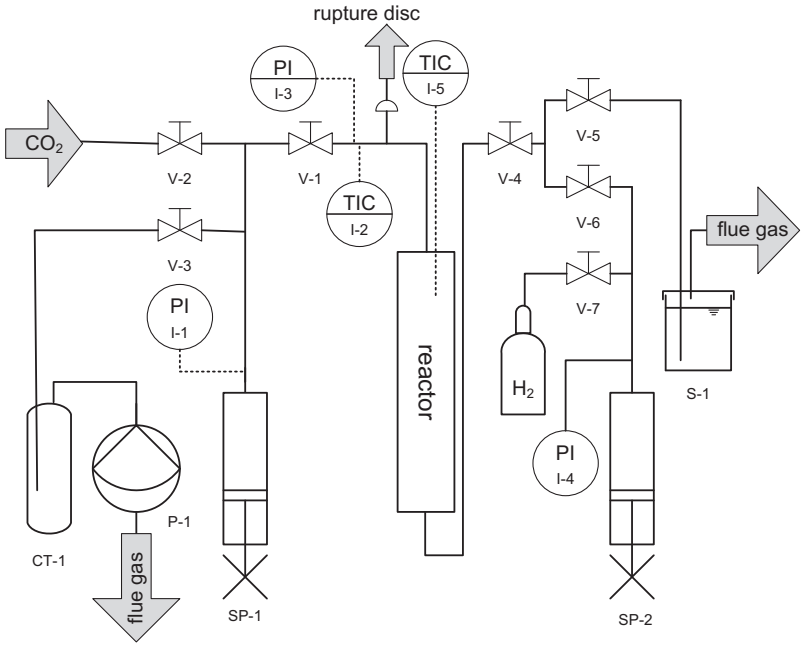

Fig. 3. Flowchart of the experimental setup used for SFRD (supercritical fluid reactive deposition) of Cu and Pt.

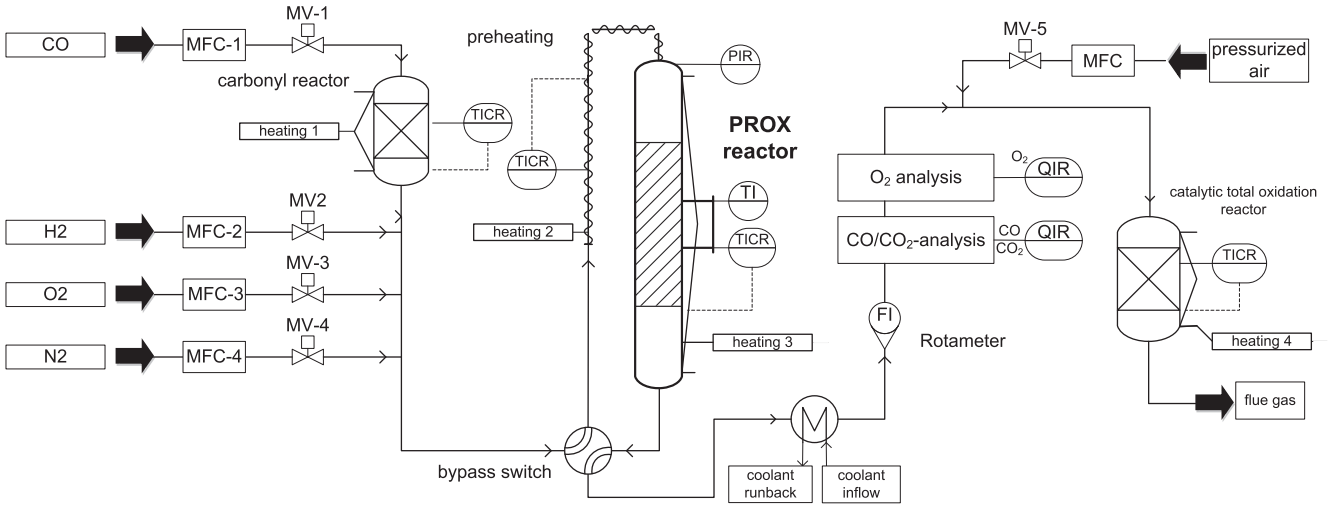

Fig. 4. Flowchart of the PROX reaction unit.

Table 1
Overview of samples under investigation.

Sample	Composition of the active layer Pt/CuO/CeO_2 (% m/m)	BET surface area (m^2/g)	Preparation method[a]	Mean CeO_2 particle diameter (nm)	Tests performed
I	0/0/100[b]	80 ± 3	Impregnation	19	H_2-TPR
II	0/100/0[c]	80 ± 3	Impregnation	–	H_2-TPR
III	0/16/84[c]	80 ± 3	Impregnation	–	H_2-TPR
IV	0/4.47/95.53	80 ± 3	Impregnation		PROX
V	0.04/4.33/95.63[c]	80 ± 3	SFRD	–	H_2-TPR, ICP-OES
VI	0.02/3.83/96.15[c]	80 ± 3	SFRD	–	CO-TPD CO_2-TPD PROX-TOS
VII	0.65/4.16/95.19[c]	80 ± 3	SFRD	19	SEM, EDX
VIII	0.02/4.49/95.49[c]	80 ± 3	SFRD	–	PROX, ICP-OES
IX	0.01/2.03/97.96[c]	80 ± 3	SFRD	–	PROX
X	0.03/5.83/94.14[c]	80 ± 3	SFRD	–	PROX
XI	0.03/3.90/96.07[c]	80 ± 3	SFRD	–	PROX (H_2O, CO_2)
XII	0.11/4.48/95.41[d]	80 ± 3	SFRD	–	STEM HAADF, EDX
XIII	0.02/4.5/95.48	80 ± 3	SFRD	–	PROX

[a] Referring to the addition of Cu.
[b] After final calcination in air at 400 °C.
[c] After final calcination in air at 450 °C.
[d] Prepared on planar α-Al_2O_3 support.

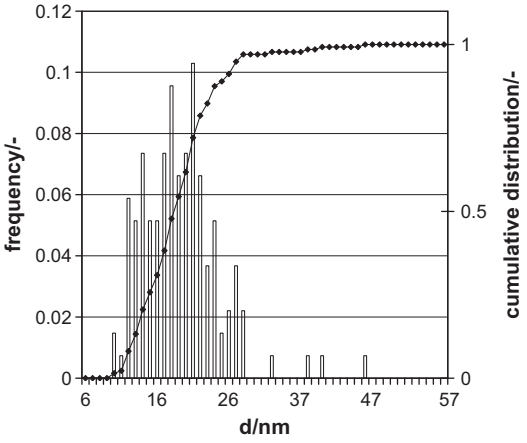

Fig. 5. Size distribution of CeO_2-particles in sample I (CeO_2 wash-coat).

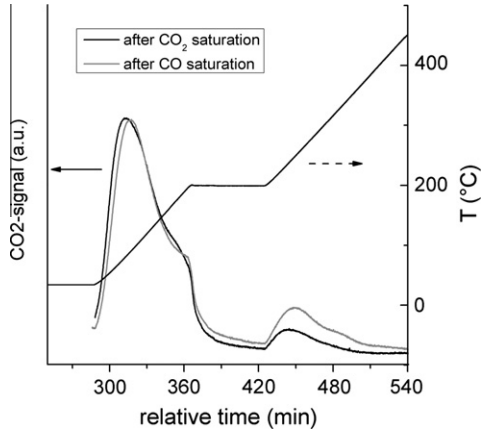

Fig. 6. CO_2-TPD curves after saturation of sample VI with CO_2 (black) and with CO (gray).

line), respectively. Both experiments were carried out with oxygen-free feed gases. However, in the latter case using CO as a sorbate, no CO was detected in the effluent, indicating that CO is readily oxidized to CO_2 with oxygen stemming from the ceria layer

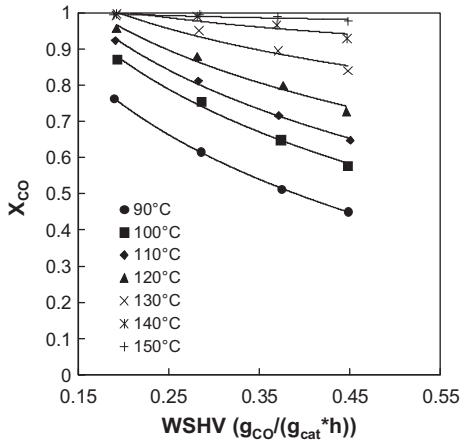

Fig. 7. Conversion of CO versus space velocity over catalyst sample IX at different reactor temperatures T_R. Symbols represent measured values, and lines fitted curves. Feed composition: 0.5% CO, 0.5% O_2, 41% H_2, 58% N_2.

and the copper oxide. The desorption profiles of CO_2 are almost congruent irrespective of the sorbate used. They exhibit a low-temperature peak at 80–90 °C and a further peak around 240 °C. According to Bueno-Lopez et al., the high-temperature peak is associated with the desorption of CO_2 from sites on pure, uncovered ceria particles [21]. If this interpretation holds, the low-temperature peak should be indicative of ceria covered with copper and platinum.

3.3. PROX performance

The conversion of CO to CO_2 over catalyst samples VIII, IX, and X as a function of the weight-hourly space velocity is plotted in Figs. 7–9 for reaction temperatures between 90 °C and 150 °C. As expected, the conversion increases with increasing temperature and decreasing space velocity. At low space velocities, sample IX (Fig. 7) shows the highest conversion; the CO-concentration can be reduced down to 12 ppm at 140 °C. Taking into account higher space velocities, sample VIII (Fig. 8) is the most active catalyst. The higher activity compared to sample IX is attributed to the higher copper content. However, too high copper loadings may result in

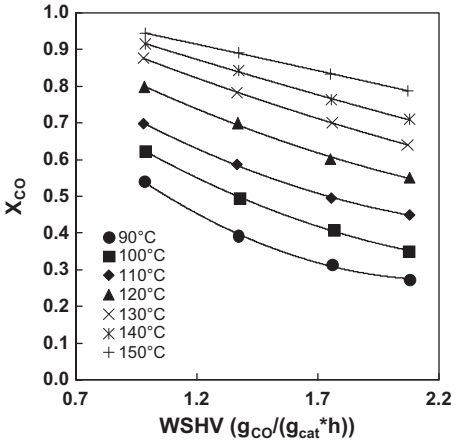

Fig. 8. Conversion of CO over catalyst sample VIII versus space velocity at different reactor temperatures T_R. Symbols represent measured values and lines fitted curves. Feed composition: 0.5% CO, 0.5% O_2, 41% H_2, 58% N_2.

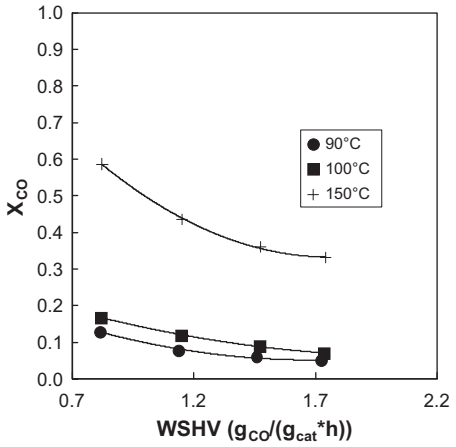

Fig. 9. Conversion of CO over catalyst sample X versus space velocity at different reactor temperatures T_R. Symbols represent measured values and lines fitted curves. Feed composition: 0.5% CO, 0.5% O_2, 41% H_2, 58% N_2.

a loss of dispersion and, consequently, in a deterioration of the activity. In our catalyst series, sample X with the highest copper content performs worse than samples IX and VIII (Fig. 9). This finding is in accordance with results reported by Dong et al. [22] who found the maximum surface capacity before dispersion drops to be at around 0.012 mmol CuO per m^2 of CeO_2 surface area. Sample X has a loading of 0.015 mmol/m^2, while samples VIII and IX stay below that limit with sample VIII coming closest with 0.0115 mmol/m^2. The first-order rate coefficients k_m have been calculated and summarized in Table 2. The data show that sample VIII is the most active catalysts at all temperatures inspected.

Comparison of the data of these catalysts (and of others not shown here) indicates that both, the highest activity and the best selectivity, correspond with an optimum composition of the active layer of about 4.5 wt.% $m_{CuO}/(m_{CuO} + m_{Pt} + m_{CeO2})$. For the best catalyst under investigation (sample VIII), Fig. 10 shows plots of the selectivity of CO as a function of the space velocity (left) and as a function of the CO-conversion (right). The selectivity deteriorates with increasing temperature. The decrease in selectivity is especially pronounced between 120 °C and 130 °C. From 90 °C to 120 °C, the selectivity is largely unaffected by space velocity. From 130 °C to 150 °C, though, the selectivity decreases with decreasing space velocity, i.e., with increasing residence time. The right graph

Table 2
Activity of CuO/CeO_2 samples.

T_R (°C)	Activity parameter k_m (ml/(g s))			
	Sample IX	Sample VIII	Sample X	Sample IV
90	15.9	37.9	5.4	14.8
100	23.7	51.2	7.9	25.5
110	29.4	71.2	–	35.7
120	38.0	98.9	–	40.6
130	54.9[a]	130.1	–	49.7[a]
140	83.3[a]	164.1	–	73.4[a]
150	116.5[a]	209.3	44.0	108.4[a]

[a] Values obtained at $X_{CO} > 70\%$.

shows that the selectivity of O_2 to CO_2 is depending on the CO-conversion, especially at temperatures higher than 120 °C and at conversions of CO higher than 70%. These observations point to two conclusions. First, the H_2-oxidation is more strongly accelerated by rising temperature than the competing CO oxidation. This means that the H_2-oxidation exhibits a higher overall activation energy than the CO oxidation. Second, the influence of the CO-conversion on the selectivity may be caused by a scarcity of CO while H_2 still is abundantly available. An effect due to a depletion of O_2 can be ruled out. A doubling of the air ratio to $\lambda = 4$ on sample VIIII at 150 °C and the lowest WHSV shown in Fig. 10 resulted in no increase in CO-conversion but rather in an increase in the O_2 consumption (data not shown). Therefore, only the oxidation of H_2 is accelerated at higher O_2 concentrations.

3.4. TOS behavior

The long-term stability of the catalysts was vicariously examined on sample XIII (see Fig. 11). The level of CO-concentration stayed between 3800 ppm over the course of a week. The slight variation observed is attributed to a long-term drift of the online measurement.

3.5. Sensitivity to water and CO_2

In a real-life PROX unit operation, the effluent coming from the water–gas shift stage still contains water and CO_2. Therefore, it is necessary to take into account a possible deterioration of PROX-activity. Fig. 12 shows the effects of CO_2 and H_2O in the feed. The presence of CO_2 lowers the conversion of CO. The decline of conversion is especially steep up to 2%. It then appears to asymptotically approach a constant conversion. This behavior points to an inhibition by adsorption of CO_2. It has previously been attributed to carbonate formation at the interfacial site otherwise responsible for forming Cu^+-carbonyl species [23]. The relative loss of conversion is less at higher temperatures. This can be explained by looking at Fig. 6. Herein, desorption of CO_2 progresses with rising temperature, i.e., the equilibrium surface coverage is lower at higher temperature.

The detrimental effect of water in terms of a relative loss of conversion at $T \leqslant 100$ °C is equally strong as in the case of CO_2. Although at the temperatures of 120 °C and 150 °C, the catalyst is more tolerant toward water. The inhibiting effect of water has been attributed to a simple blocking of the catalyst surface by molecular water [23].

To the best of our knowledge, the $PtCuO/CeO_2$ catalysts presented here belong to the best PROX-catalysts reported so far. For comparison, Fig. 13 shows conversion data of sample VIII as a function of the modified residence time together with the best literature data. An overview of the preparation methods applied is given in Table 3. Unfortunately, it was common use in studies previously reported in the literature to vary the temperature, only,

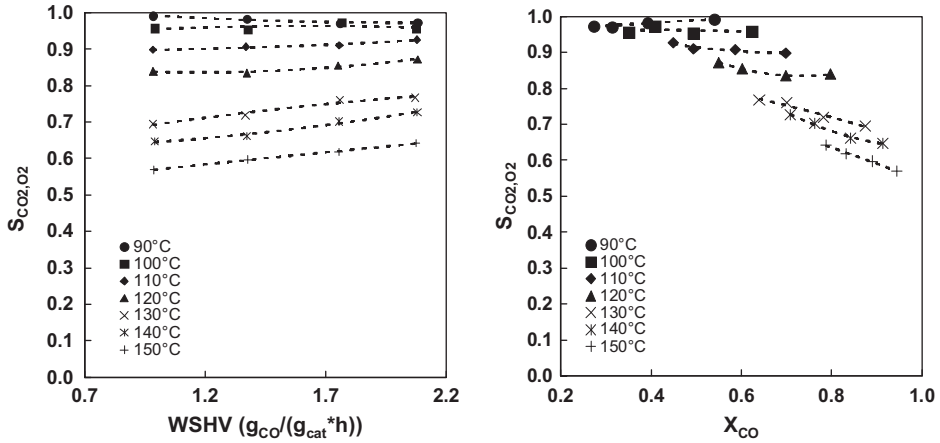

Fig. 10. Selectivity of O_2 to CO_2 at different space velocities and temperatures (left) and selectivity of O_2 to CO_2 versus conversion of CO at different temperatures (right) on sample VIII. Symbols represent measured data and dashed lines data trends.

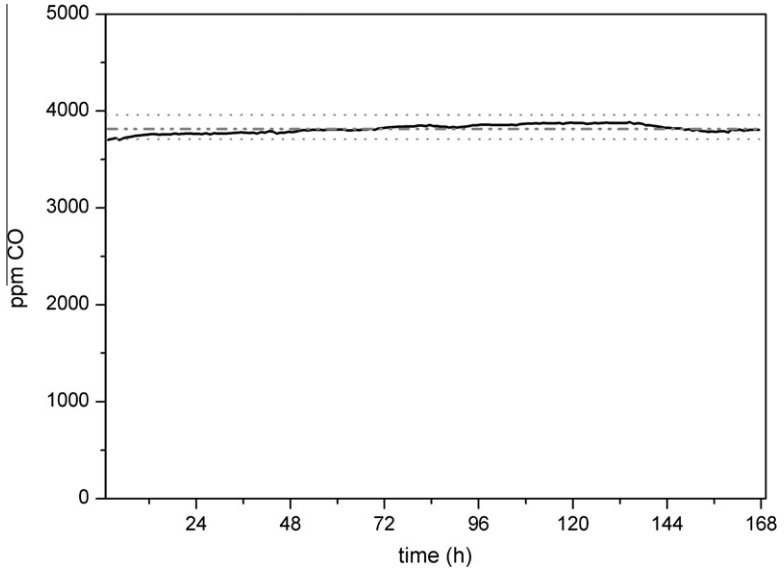

Fig. 11. Time on stream for catalyst sample VI at 333 ml_{NTP}/min and T_R = 100 °C. Feed composition: 0.5% CO, 0.5% O_2, 41% H_2, 58% N_2. The dotted lines give the confidence interval.

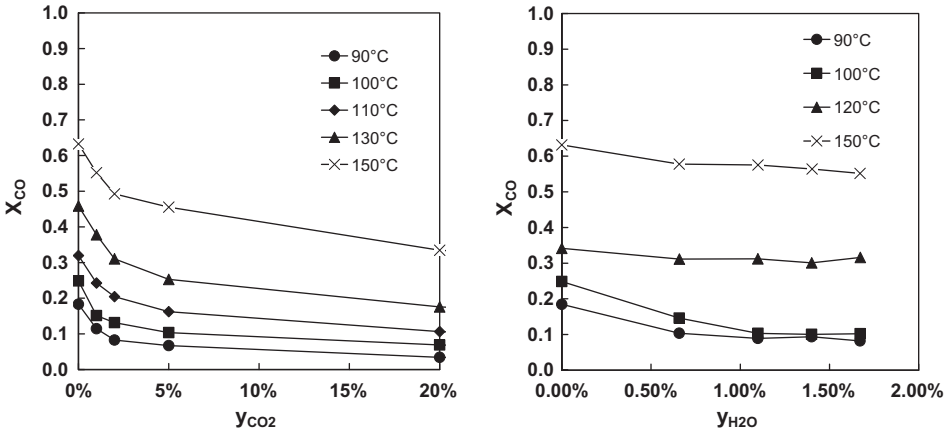

Fig. 12. Variation of CO_2 content (left) and H_2O content (right) in the PROX feed on sample XI at 800 ml_{NTP}/min and various temperatures. Feed composition: 0.5% CO, 0.5% O_2, *y*% CO_2 (H_2O respectively), 41% H_2, (58%-*y*) N_2.

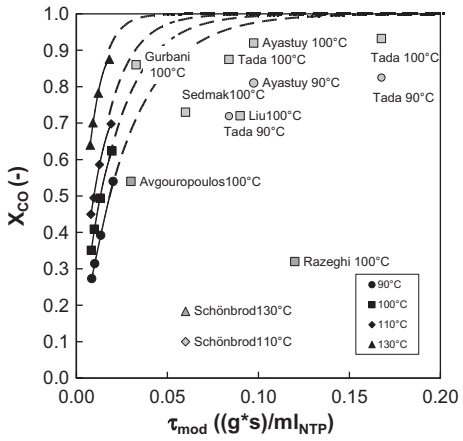

Fig. 13. Conversion of CO versus modified residence time over $PtCuO/CeO_2$ (this work, sample VIII, black symbols) and over CuO/CeO_2 catalysts reported in the literature (gray symbols). Symbols represent measured data; lines stem from a first-order fit of the kinetics over our own catalyst (sample VIII). Feed composition: 0.5% CO, 0.5% O_2, 41% H_2, 58% N_2.

Table 3
Overview of catalysts and preparation methods applied by other authors (performances are compared in Fig. 13).

Author	Composition $m_{CuO}/(m_{CuO} + m_{CeO2})$[a] (%)	Preparation method
Avgouropoulos and Ioannides [24]	6.44	Combustion method
Ayastuy et al. [25]	6.8	Wet impregnation/ monolith
Gurbani et al. [12]	8.61	Deposition precipitation
Liu et al. [26]	12.75	Urea gelation/co-precipitation (UGC)
Razeghi et al. [27]	5	Co-precipitation
Schönbrod et al. [28]	10.36	Co-precipitated urea
Sedmak et al. [29]	4.89	Sol–gel peroxo route
Tada et al. [30]	7.34	CETAB

[a] Calculated from literature under the assumption of fully oxidized copper and cerium.

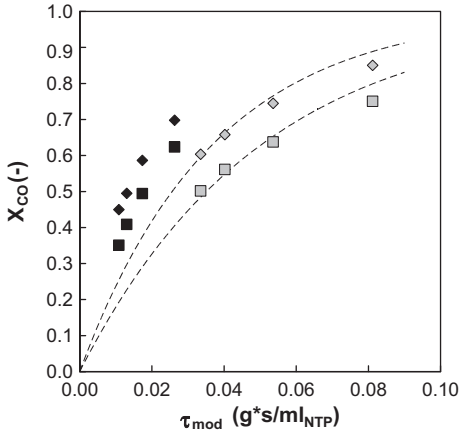

Fig. 14. Comparison of CO-conversion on catalysts VIII (black) and IV (gray) at 100 °C (squares) and 110 °C (diamonds), respectively. Also shown are modeled conversions at both temperatures on catalyst IV for a simple first-order reaction rate (dashed lines).

while the residence time was fixed, or to adjust the residence times such that full conversion was achieved. As a result, the literature data plotted in Fig. 13 cover a different regime of residence times

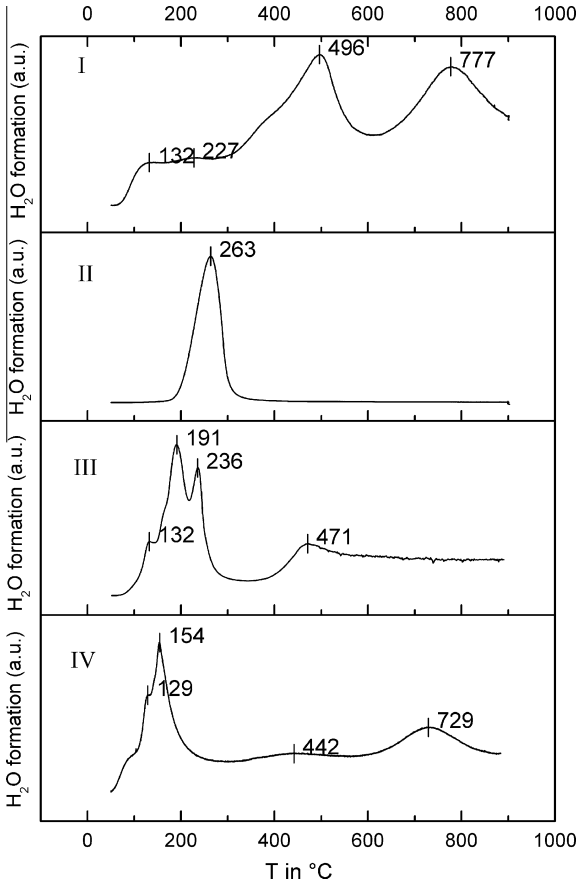

Fig. 15. Formation of water as a function of the reduction temperature upon TPR with H_2 of sponge samples coated with (I) pure CeO_2 (sample I), (II) wet chemically prepared CuO (sample II), (III) wet chemically prepared CuO/CeO_2 (sample III) and (IV) SFRD-prepared $PtCuO/CeO_2$ (sample V).

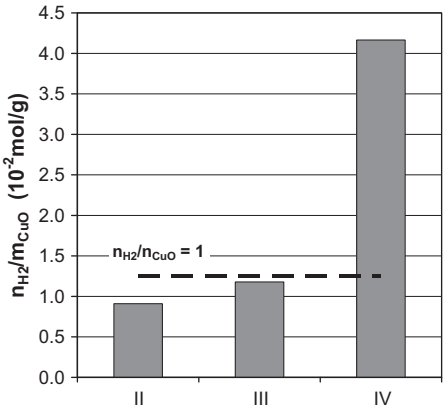

Fig. 16. Amount of H_2 consumed by H_2-TPR depicted in Fig. 15 related to the CuO mass of the samples. The dashed line shows the stochiometric maximum. For the sake of comparability only H_2-consumption in the temperature range between 50 °C and 360 °C was taken into account.

than our own data. Nevertheless, it can be seen that our sample VIII is very active, while only the catalyst reported by Gurbani et al. [12] showed a slightly higher activity at 100 °C. This high activity is attributed to a high dispersion of copper of 87%. Extrapolation of the kinetic fit toward higher residence times – as shown in Fig. 13 through the dotted parts of the lines – gives an indication of the conversion differences in the complete range of residence

Table 4
Data from H_2-TPR measurements.

Sample	Sample mass (g)	Consumed amount H_2 (mol)	n_{H2}/n_{CuO} (–)
CeO_2 I	0.883	3.35E−05	–
CuO II	0.837	1.93E−04	0.72
CuO/CeO_2 III	0.854	1.75E−04	0.94
$PtCuO/CeO_2$ IV	0.544	2.53E−05	3.31

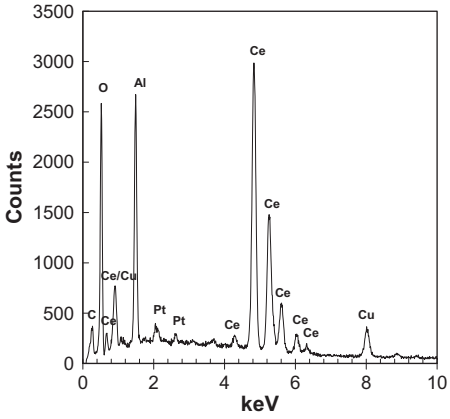

Fig. 17. EDX-spectrum of sample VII ($PtCuO/CeO_2$).

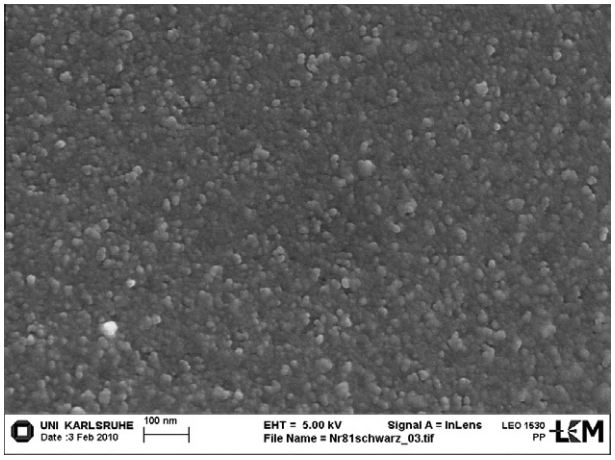

Fig. 18. SEM image of the surface of sample VII ($PtCuO/CeO_2$).

times. Fig. 14 offers a comparison between SFRD-created sample VIII and sample IV prepared via impregnation. Also shown is an extrapolation of sample IV data according to first-order kinetics. Although both samples contain the same percentage of copper oxide per mass, the SFRD-prepared sample VIII exhibits a much higher activity.

3.6. Reducibility

Searching for an explanation for the excellent performance of the $PtCuO/CeO_2$ catalysts prepared by means of SFRD, temperature-programmed reduction experiments were carried out. The reducibility of the copper species in CuO/CeO_2 catalyst is known to increase with increasing dispersion of the copper species, and low reduction temperatures are correlated with high PROX-activity [1,31–33].

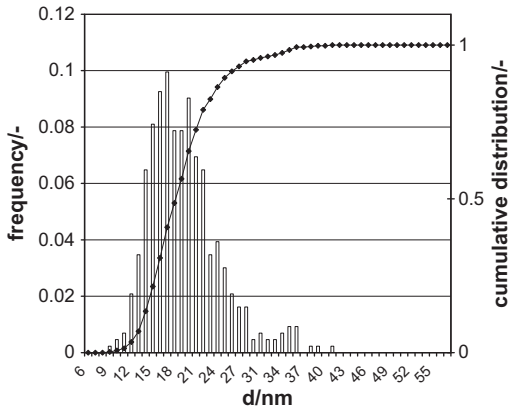

Fig. 19. Size distribution of 432 CuO- and CeO_2-particles in sample VII ($PtCuO/CeO_2$).

In Fig. 15, TPR-plots of sponges coated only with either CeO_2 or CuO (plots I and II) are compared with plots of $(Pt)CuO/CeO_2$ sponge catalysts. The TPR-spectrum of the pure ceria wash-coat shows two peaks, one at 497 °C attributed to the reduction of surface ceria and one at 777 °C due to bulk ceria reduction [34]. Plot II stemming from CuO deposited by means of wet-chemical impregnation of the blank sponge exhibits a single reduction peak at 263 °C. The TPR-pattern changes if CuO is deposited on a CeO_2 wash-coat as shown in plot III. The reduction peaks at 132 °C, 191 °C, and 236 °C (III), denoted as α, β, and β′ peaks in the literature, are attributed to the presence of more easily reducible surface (α, β) and bulk (β′) species of copper oxide [34–36]. The peak at 471 °C in plot III stems from uncovered ceria and is usually denoted as γ. In literature, strong metal oxide-support interactions (SMSI) are found to be responsible for the decrease in reduction temperature and the increase in peak complexity [37]. The bottom plot in Fig. 15 has been taken from a sponge coated with $PtCuO/CeO_2$, where Cu and Pt were deposited by means of SFRD. In this TPR-spectrum, the reduction peaks of CuO are clearly shifted to lower temperatures. Furthermore, as Fig. 16 reveals, the H_2-uptake per mass of copper (II) oxide increases in the order $CuO < CuO/CeO_2 < PtCuO/CeO_2$. This means that in the case of the SFRD-prepared catalyst, the available copper is more efficient in consuming H_2. However, only in the case of the SFRD-prepared catalyst does the H_2-consumption exceed the theoretically necessary amount for total reduction of CuO (see Table 4). Therefore, the CuO on samples II and III is not fully reduced at temperatures up to 360 °C. On sample IV, the amount of H_2 consumed would be more than enough to fully reduce the CuO contained. Hence, a good part of CeO_2 has to have been reduced as well. It is assumed that in order to allow for the reduction of ceria at temperatures up to 360 °C, intimate contact between Cu^+/Cu^{2+} and Ce^{3+}/Ce^{4+} species is required to establish a redox cycle [38–40]. Thus, a high H_2-consumption as is the case on the SFRD-prepared sample additionally points to a high dispersion of Cu-species on CeO_2.

However, a close inspection of the literature on Cu-based PROX-catalysts shows that the reducibility of the copper species is also influenced by the addition of potassium ions [31], by the amount of copper loaded [34,41] and by the application of different preparation methods [32,33,35,42].

Jung et al. [43] showed that Pt-doping at 0.05 wt.% of a 5 wt.% $CuO–CeO_2$ resulted in the appearance of an additional reduction peak in the low-temperature range and a slight shift of the peaks attributed to copper species to lower temperatures. Nevertheless, the highest peak in the low-temperature range still is at about 200 °C.

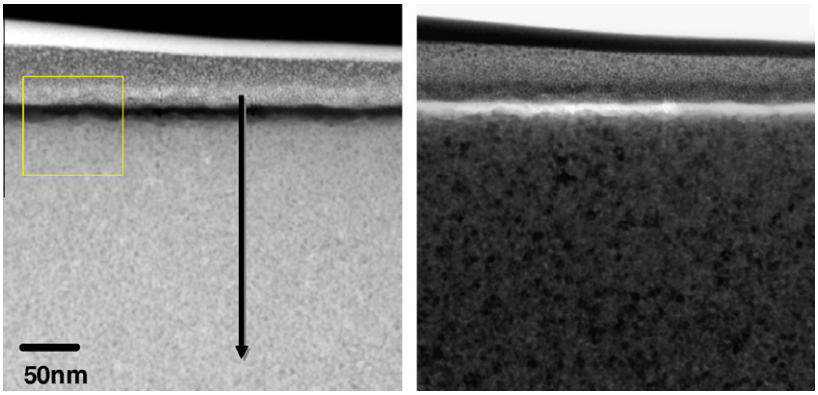

Fig. 20. STEM dark field (left) and bright field (right) images of FIB milled cross-sectional area of catalyst sample XII. The black arrow marks the path of the EDX-probe.

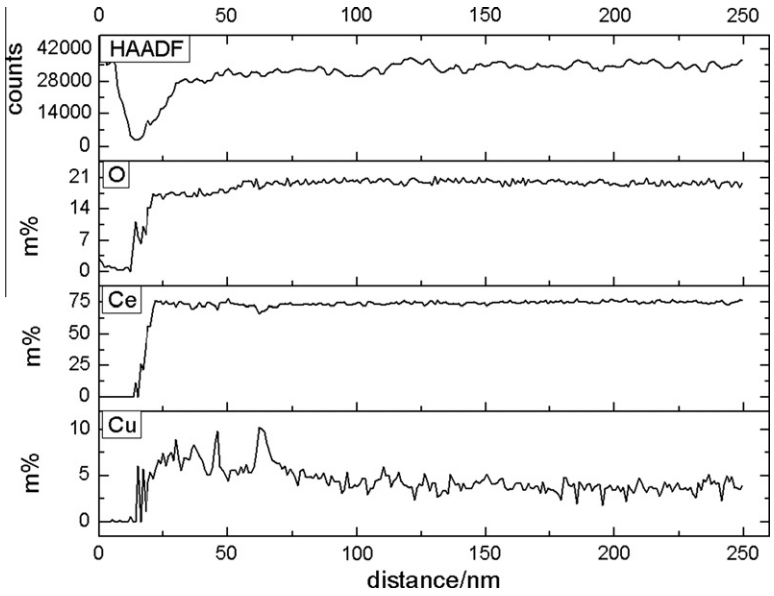

Fig. 21. Intensity of the HAADF-signal and elemental composition of sample XII as determined via EDX along the probe's path according to Fig. 20.

3.7. Size of CuO-particles

The results from TPR point to small, easily reducible CuO-particles. To this respect, the SEM image (Fig. 18) is not conclusive since particles appear rather big in size Fig. 19.

The EDX-spectrum in Fig. 17 shows an averaged elemental composition of the surface layer of a $PtCuO/CeO_2$ catalyst. However, the low spatial resolution and the overlapping Ce and Cu signals at about 0.913 keV prevent EDX analyses of individual particles to distinguish locations of CeO_2, CuO, and Pt in the samples. This was due to the amount of high energy K_α photons being too low in a beam focused on single particles to generate enough counts for the discriminating peaks at 4 keV and higher.

In Fig. 20, are shown the dark field and bright field images of the cross-section of the active layer of sample XII. The topmost layer consists of tungsten and the underlying layer consists of carbon. The application of both was a requirement during FIB-preparation. The next visible entity is a gap due to delamination that occurred during FIB-milling. Below the gap starts the ceria layer, as can be seen in Fig. 21. In this graph, the relative elemental composition from the deconvolution of the respective EDX-spectra at each nanometer of a 250 nm path is given. EDX-spectra have been evaluated with respect to the mass fraction of cerium, oxygen, copper, platinum, carbon, and tungsten, of which the latter three are not shown in Fig. 21. Unfortunately, platinum could not be detected since the noise level was too high for a platinum line to be unambiguously identified in the EDX-spectrum.

The intensity of the HAADF image is given in first row of the graph. Herein, the position of the gap is visible as a sharp drop of photon counts. Along with cerium, oxygen is clearly and constantly detectable from the gap to the end of the path. Copper is found as nanoscale structures in depths up to about 70 nm as indicated by a series of sharp peaks shown in the bottom row of Fig. 21. This shows that the ceria layer is penetrated by the dissolved copper complexes. Furthermore, the copper content diminishes with increasing depth.

These findings of nanosized copper inside and in close contact to the ceria layer give an explanation to the good reducibility and thus high activity of the catalyst. The reductive atmosphere during SFRD-preparation quite possibly further leads to close contact between copper and ceria since oxygen vacancies would be formed that are known to stabilize late transition metal nanoparticles and form a strong metal-support bonding [44,45]. The findings of STEM HAADF are in agreement with our TPR results. No bulk CuO phase could be found neither in the dark field nor bright field image where differences in atomic numbers should result in clear

contrast differences in the image. This explains the absence of the peak ascribed to bulk CuO in the H2-TPR profiles of the SFRD-prepared catalyst. Obviously, in comparison with the REM image of the catalyst surface, the image of the cross-section reveals a much finer, granular structure on the layers inside. With regard to activity loss at too high copper loadings, a possible blocking of pores could be held responsible.

Nevertheless, the role of the platinum complex is yet not fully understood. For once, it is clear that the complex is completely reduced at SFRD conditions as seen in previous work [14]. The platinum may then act as a catalyst during the reduction step at supercritical conditions facilitating the reduction of $Cu(tmhd)_2$ at 80 °C. From this point of view, platinum is beneficial during the preparation and is simply allowing for highly dispersed copper species that are in turn responsible for the high activity shown. From a second point of view, Pt may also serve as a dopant to the CuO/CeO_2-catalyst as Jung et al. [43] found out for Pt contents of 0.05wt% and higher. In contrast to these findings, Tada et al. [30] reported the addition of Pt to CuO/CeO_2 to reduce CO-conversion.

4. Conclusions

$PtCuO/CeO_2$ catalysts prepared by means of SFRD and supported on α-Al_2O_3 sponges exhibit high activity and selectivity in the preferential oxidation of CO in a large excess of hydrogen. It was possible to reduce the CO-concentration from 5000 ppm to 12 ppm at 140 °C. The best among the catalysts produced by means of SFRD exhibited an activity two times as high as a reference sample prepared by conventional wet-chemical impregnation with copper. The high activity is attributed to a high dispersion of copper species in the ceria layer.

The presence of platinum has a beneficial effect on the performance of the catalysts prepared by means of SFRD, but its actual role is not fully understood, yet. We assume that platinum catalyses the low-temperature reduction of the copper complex during the preparation of the catalyst by means of SFRD. However, it could also be possible that Pt acts as a promoter in the PROX reaction.

Three different copper loadings have been analyzed of which the second highest loading proved to be the most active. In accordance with literature data, we assume that activity increases with the copper loading up to an optimum. Beyond that optimum, the catalyst performance deteriorates.

It was furthermore shown that CO_2 and H_2O present in the reactor feed both reduce the catalyst's activity and that the effect diminishes with rising temperature. The SFRD-prepared catalyst was shown to be stable for up to a week of continuous operation.

Acknowledgments

The authors thank the German Research Foundation (DFG) for financial support. Dr. Reinhard Schneider and Peter Pfundstein (LEM, Karlsruhe Institute of Technology) are acknowledged for taking the electron micrographs and EDX measurements.

References

[1] W. Liu, M. Flytzani-Stephanopoulos, J. Catal. 153 (1995) 304.
[2] X. Wang, J.C. Hanson, D. Gamarra, A. Martinez-Arias, J.A. Rodriguez, M. Fernandez-Garcia, J. Phys. Chem. B 110 (2006) 428.
[3] P. Djinovic, J. Batista, A. Pintar, Appl. Catal. Al 347 (2008) 23.
[4] P. Djinovic, J. Batista, A. Pintar, Catal. Today 147S (2009) 191.
[5] W. Liu, M. Flytzani-Stephanopoulos, C. Wadia, Catal. Today 28 (1996) 391.
[6] P. Bera, S.T. Aruna, K.C. Patil, M.S. Hegde, J. Catal. 186 (1999) 36.
[7] W.-J. Shen, Y. Ichihashi, Y. Matsumura, Catal. Lett. 83 (2002) 33.
[8] S. Hocevar, J. Batista, J. Levec, J. Catal. 184 (1999) 39.
[9] G. Avgouropoulos, T. Ioannides, Appl. Catal. A 244 (2003) 155.
[10] R.J. Farrauto, W. Ruettinger, O. Ilinich, L. Shore, Y. Liu, T. Giroux, Catal. Rev.-Sci. Eng. 49 (2007) 141.
[11] D. Gamarra, G. Munuera, A.B. Hungria, M. Fernandez-Garcia, J.C. Conesa, P.A. Midgley, X.Q. Wang, J.C. Hanson, J.A. Rodriguez, A. Martinez-Arias, J. Phys. Chem. C 111 (2007) 11026.
[12] A. Gurbani, J.L. Ayastuy, M.P. Gonzalez-Marcosa, J.E. Herrero, J.M. Guil, M.A. Gutierrez-Ortiz, Int. J. Hydrogen Energy 34 (2009) 547.
[13] A. Martinez-Arias, M. Fernandez-Garcia, O. Galvez, J.M. Coronado, J.A. Anderson, J.C. Conesa, J. Soria, G. Munuera, J. Catal. 195 (2000) 207.
[14] G. Incera Garrido, F.C. Patcas, G. Upper, M. Türk, S. Yilmaz, B. Kraushaar-Czarnetzki, Appl. Catal. A 338 (2008) 58.
[15] A. Cabañas, J.J. Watkins, J.M. Blackburn, D.P. Long, Science 294 (2001) 141–145.
[16] Y. Zhang, C. Erkey, J. Supercrit. Fluids 38 (2006) 252.
[17] G. Incera Garrido, F.C. Patcas, S. Lang, B. Kraushaar-Czarnetzki, Chem. Eng. Sci. 63 (2008) 5202.
[18] B. Dietrich, G. Schell, E.C. Bucharsky, R. Oberacker, M.J. Hoffmann, W. Schabel, M. Kind, H. Martin, Int. J. Heat Mass Transfer 53 (2010) 198.
[19] B. Dietrich, M. Kind, H. Martin, Proc. 14th Intern. Heat Transfer Conf. IHTC 14 August 08–13, 2010, Washington, DC, USA.
[20] F. Zhang, S.-W. Chan, J.E. Spanier, E. Apak, Q. Jin, R.D. Robinson, I.P. Herman, Appl. Phys. Lett. 80 (2002) 127.
[21] A. Bueno-Lopez, K. Krishna, M. Makkee, Appl. Catal. A 342 (2008) 144.
[22] L. Dong, Y. Hu, M. Shen, T. Jin, J. Wang, W. Ding, Y. Chen, Chem. Mater. 13 (2001) 4227.
[23] D. Gamarra, A. Martínez-Arias, J. Catal. 263 (2009) 189–195.
[24] G. Avgouropoulos, T. Ioannides, Catal. Lett. 116 (2007) 1.
[25] J.L. Ayastuy, N.K. Gamboa, M.P. González-Marcos, M.A. Gutiérrez-Ortiz, Chem. Eng. J. 171 (2011) 224–231.
[26] Y. Liu, Q. Fub, M.F. Stephanopoulos, Catal. Today 93–95 (2004) 241.
[27] A. Razeghi, A. Khodadadi, H. Ziaei-Azad, Y. Mortazavi, Chem. Eng. J. 164 (2010) 214–220.
[28] B. Schönbrod, F. Marino, G. Baronetti, M. Laborde, Int. J. Hydrogen Energy 34 (2009) 4021.
[29] G. Sedmak, S. Hocevar, J. Levec, J. Catal. 213 (2003) 135.
[30] M. Tada, R. Bal, X. Mu, R. Coquet, S. Namba, Y. Iwasawa, Chem. Commun. 44 (2007) 4689.
[31] Z. Liu, R. Zhou, X. Zheng, Int. J. Hydrogen Energy 33 (2008) 791.
[32] G. Avgouropoulos, T. Ioannides, H. Matralis, Appl. Catal. B 56 (2005) 87.
[33] S.-M. Zhang, W.-P. Huang, X.-H. Qiu, B.-Q. Li, X.-C. Zheng, S.-H. Wu, Catal. Lett. 80 (2002) 41.
[34] F. Marino, B. Schönbrod, M. Moreno, M. Jobbágy, G. Baronetti, M. Laborde, Catal. Today 133–135 (2008) 735.
[35] F. Marino, G. Baronetti, M. Laborde, N. Bion, A. Le Valant, F. Epron, D. Duprez, Int. J. Hydrogen Energy 33 (2008) 1345.
[36] Z. Liu, R. Zhou, X. Zheng, J. Mol. Catal. A: Chem 267 (2007) 137.
[37] A. Pintar, P. Djinovic, J. Batista, Appl. Catal. A 347 (2008) 23–33.
[38] M. Fernandez-Garcia, A. Hornes, P. Bera, Zs. Koppany, Z. Schay, A. Martinez-Arias, D. Gamarra, Catal. Today 143 (2009) 211–217.
[39] M.-F. Luo, Y.-J. Zhong, X.-X. Yuan, Appl. Catal. A 162 (1997) 121–131.
[40] R. Pirone, G. Russo, T. Caputo, L. Lisi, Appl. Catal. A 348 (2008) 42–53.
[41] C.G. Maciel, M. Naceur Belgacem, J. Mansur Assaf, Catal. Lett. 141 (2011) 316.
[42] X.-C. Zheng, X.-L. Zhang, X.-Y. Wang, S.-H. Wu, React. Kinet. Catal. Lett. 92 (2) (2007) 195.
[43] C.R. Jung, A. Kundu, S.W. Nam, H.-I. Lee, Appl. Catal. A 331 (2007) 112.
[44] C.T. Campbell, C.H.F. Peden, Science 309 (2005) 713.
[45] J.A. Farmer, C.T. Campbell, Science 329 (2010) 933.